Inversion of the Gravity Gradiometry Data by ResUnet Network: An Application in Nordkapp Basin, Barents Sea

Zhengwei Xu, Rui Wang, Michael S. Zhdanov, *Member, IEEE*, Xuben Wang, Jun Li, Bing Zhang, Shengxian Liang, and Yang Wang

***Abstract*— The study and assessment of the subsurface density distribution are vital for mining and oil and gas exploration. This can be achieved by the 3-D inversion of the observed gravity and gravity gradiometry (GG) data. Due to the ill-posedness of the geophysical inverse problem, the nonuniqueness and instability of solutions represent the main difficulties in inversion. In recent years, convolutional neural networks, especially U-net technology, have found wide applications in image processing, recognition, and reconstruction. This article proposes using this method for fast reconstruction of the subsurface density models based on the ResUnet technology. The developed new method was examined on two 3-D synthetic gravity and GG datasets inversion. The results show that the ResUnet network can reconstruct the density anomaly with sharp boundaries and is robust to the noise, making the solution stable.**

***Index Terms*— 3-D inversion, gravity and gravity gradiometry (GG), ResUnet.**

I. Introduction

THE reconstruction of subsurface density distribution is routinely used for mapping geological formations in mineral, geothermal, and hydrocarbon exploration. The density model helps improve seismic velocity models for imaging salt and basalt structures. In addition, independent measurements of the gravity field and gravity gradiometry (GG) data are extensively used for determining 3-D density models in regional geological settings.

Manuscript received 24 October 2022; revised 30 January 2023 and 6 March 2023; accepted 24 April 2023. Date of publication 28 April 2023; date of current version 22 May 2023. This work was supported in part by the National Natural Science Foundation of China under Grant 41930112 and Grant 42274132, in part by the Natural Science Foundation of Jilin Provincial under Grant 20200201053JC, and in part by the Innovation and Development Strategy Research Project of Science and Technology Department of Jilin Province under Grant 20220601157FG. *(Corresponding author: Rui Wang.)*

Zhengwei Xu, Xuben Wang, Jun Li, Bing Zhang, and Shengxian Liang are with the Key Laboratory of Earth Exploration and Information Techniques, Ministry of Education, College of Geophysics, Chengdu University of Technology, Chengdu 610059, China (e-mail: zhengwei.xu@cdut.edu.cn; wxb@cdut.edu.cn; lijun3@cdut.edu.cn; zhangb@cdut.edu.cn; liangshengxian626@163.com).

Rui Wang is with the School of Computer Science and Technology, Changchun University of Science and Technology, Changchun 130022, China (e-mail: rwang@cust.edu.cn).

Michael S. Zhdanov is with the Consortium for Electromagnetic Modeling and Inversion (CEMI), The University of Utah, Salt Lake City, UT 84112 USA, and also with TechnoImaging, Salt Lake City, UT 84107 USA (e-mail: michael.s.zhdanov@gmail.com).

Yang Wang is with the Key Laboratory of Geophysics, SINOPEC Geophysical Research Institute, Nanjing 130022, China (e-mail: wangyang.swty@sinopec.com).

Digital Object Identifier 10.1109/TGRS.2023.3271606

Over the last decades, many publications have been dedicated to regularized inversion of gravity and GG data [1], [2], [3], [4], [5], [6], [7], [8], [9], [10], [11]. For example, articles [2], [12], [13], [14] present the smooth solutions of gravity field inversion based on the minimum norm and maximum smoothness stabilizing functionals. However, the results of smooth inversion usually have low contrast compared to true geology, which makes smooth inverse models poor approximations of the real geological structures.

It was demonstrated by Zhdanov [6], [7] that regularized solution of an ill-posed inverse problem can be produced by special stabilizing functionals enforcing the sharp boundaries of the density contrast within the inverse models. For example, Portniaguine and Zhdanov [15] proposed focusing regularization inversion method to resolve the shape of the density anomalies by minimizing the areas with large gradients. This method was successfully applied to gravity inversions [7], [16], [17], [18]. Another approach to recovering the blocky geological structures can be based on L1 norms and total variation minimization [6], [19], [20], [21], [22]; however, this approach generates smaller contrast images than one based on focusing regularization [6]. Xu et al. [23] proposed a novel hybrid imaging procedure to study the density contrast basin boundary to improve the resolution.

In the past decade, the idea of integrating the known geological and petrophysical data as a priori information into various geophysical inversion algorithms, such as fuzzy c-means [24], and multinary transformation [25], has attracted substantial attention. Bringing a priori information would enhance the reliability of the inverse models, making them consistent with the known geology.

Another approach to incorporating a priori geological information to solve the inverse problem is based on machine learning (ML). Several recent publications have considered using unsupervised ML algorithms to solve gravity or/and magnetic inverse problems (see [26], [27], [28]). However, unsupervised learning still requires some geological information to validate the results. In contrast, the supervised ML methods can predict the models using a priori geological information. Common types of classification algorithms, such as linear classifiers [29], [30], support vector machines [31], decision trees [32], and random forecast [33], [34], have been applied to address geophysical inverse ill-posed problems. In addition, linear regression [35], logistic regression [36], [37], and polynomial regression [38] have been successfully used to recover subsurface physical properties. However, supervised learning is limited in handling complex tasks, and the training process computation is time-consuming.

As another type of supervised learning, deep learning (DL) uses a neural network to mimic the mechanism of the human brain for analytical learning and geoscience data interpretation by understanding the relationship between the data and model properties [39], [40]. Due to its excellent capabilities in feature learning and information extraction, DL can complement traditional geophysical inversion. For example, the variations of density values, 3-D shapes, and distribution of anomalous bodies in the subsurface lead to the change of 2-D gravity observation data on the surface. The convolutional neural network (CNN) uses end-to-end learning to extract the relationships between 2-D gravity data and the 3-D density model [41], [42]. He et al. [43] proposed a novel method for depth-to-basement estimation using a CNN network and successfully applied it to the accurate delineation of sedimentary basins using gravity data.

The quantification of uncertainty in geophysical inverse problems can be accomplished through the Bayesian inference framework using Markov chain Monte Carlo (MCMC) sampling of posterior probability density [44]. Trans-dimensional MCMC has been proposed as a method for jumping into different states characterized by different model dimensions [45], [46], [47]. In the deterministic framework, uncertainty can be qualitatively assessed by varying initial or reference models [48], or quantitatively analyzed by analyzing the linearized model covariance matrix [1]. In the DL framework, Bayesian neural networks are used to estimate the posterior probability distribution of the model parameters, which provides a probabilistic interpretation of the uncertainty [49].

This study establishes the nonlinear mapping between gravity and GG field data (as the input) and the anomalous density model based on the convolution network approach. The developed method was tested on the synthetic gravity and GG field data and applied to interpreting the optimized GG data sets collected in Nordkapp Basin, Barents Sea.

II. Inversion Methodology Based on ResUnet Network

A. Generation of Training Sets

The ResUnet network is trained using a carefully constructed training set, designed to enable the network to capture comprehensive features from input gravity and GG data and build an inherent correlation with the 3-D output-labeled isolated density anomalies. To achieve this, anomalous blocks of varying sizes were arbitrarily selected and placed at different locations in the subsurface, and the corresponding gravity and GG data were generated by forward modeling. The horizontal size of the anomalies ranged along the x-axis and y-axis within 0–4000 m, and the depth range along the z-axis was 0–1000 m. The blocks were arranged with a minimum plumb distance from each face to the face of the corresponding model space. The area of inversion was discretized into 4000 cells with a uniform density of 200 $\times$ 200 $\times$ 100 m, and stations

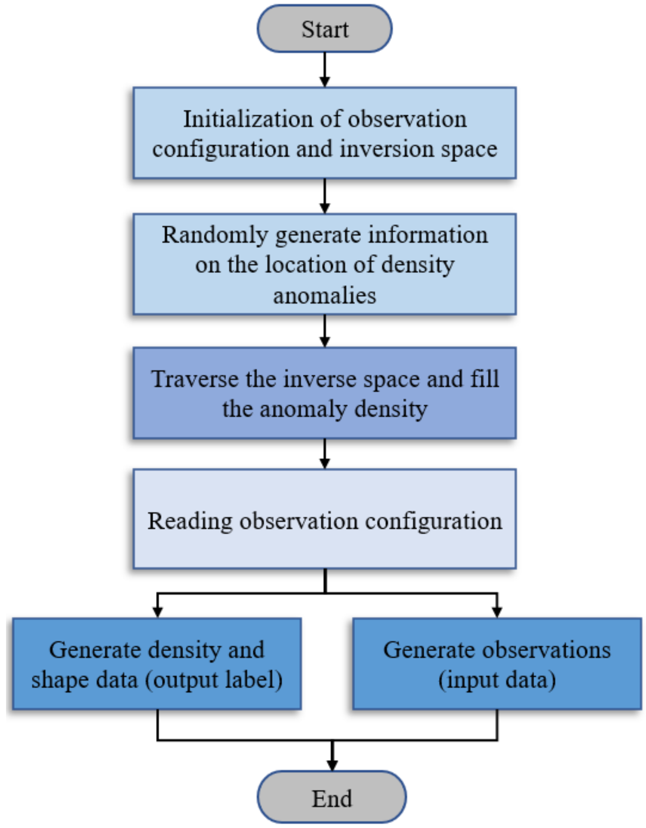

Fig. 1. Workflow of the training set generation.

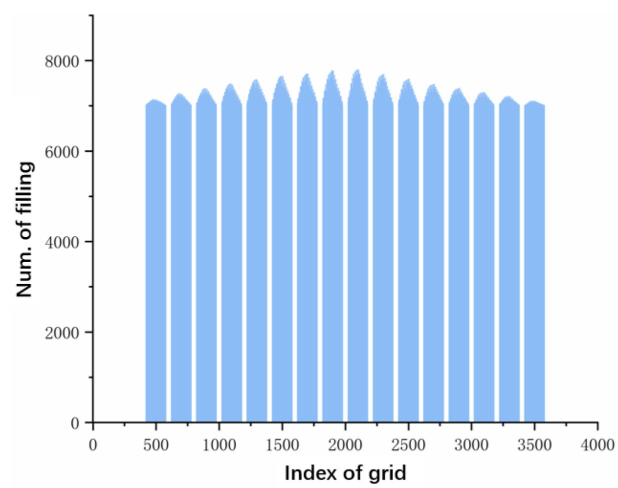

Fig. 2. Histogram of the grid filling.

were positioned along 21 survey lines with a spacing of 200 m between each line. To simulate the complexity of actual geological scenarios, the residual density of the anomalous bodies was randomly selected from the interval [−1, 1] g/cm^3. The training set generation workflow is illustrated in Fig. 1.

We divided the training data into two disjoint subsets. The training set was used to learn the parameters, such as weights and thresholds, in each layer. The other subset was used as a validation set to estimate the generalization error and update the hyperparameters through the trial-by-error method. The

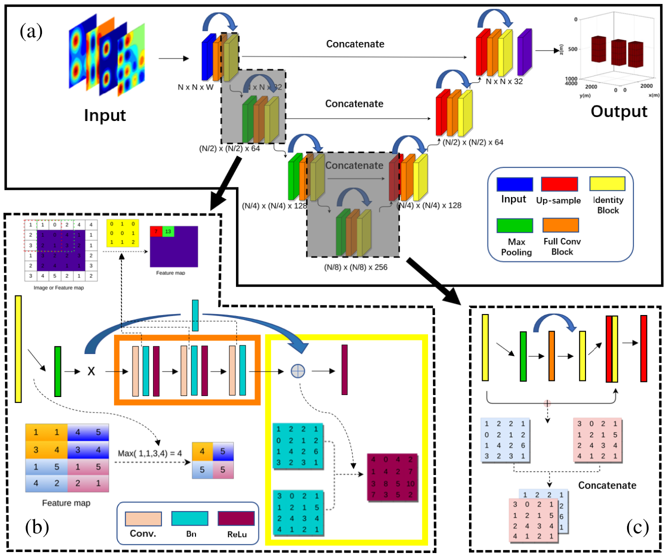

Fig. 3. (a) Overview of the structure of ResUnet network. (b) Characteristic operations of direct connection and shortcut in each step along the encoding part (modified from [43]). (c) Characteristic operations of concatenating between layers along encoding and decoding parts.

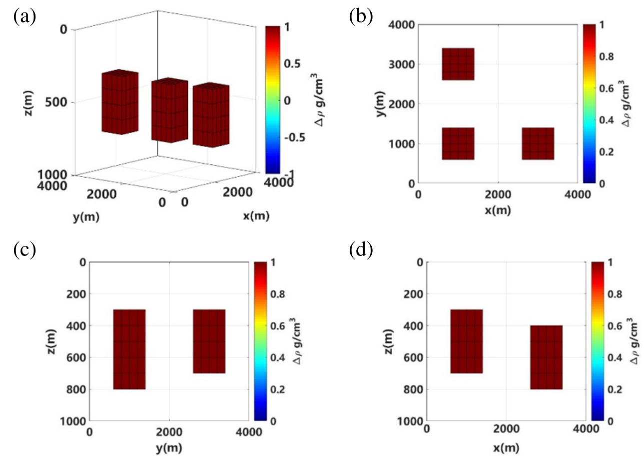

Fig. 4. (a) 3-D view model 1. (b) Y–Z view model. (c) X–Y view model. (d) X–Z view model.

hyperparameters, including convolutional layer parameters, pooling layer parameters, network depth, and network width, followed the classical network structure parameters of U-net and ResNet. We used 11 903 training models as output labels and corresponding surface gravity and GG responses as input labels. We randomly selected 80% of the data for the training and validation sets, and the remaining data were used for testing. To prevent overfitting and underfitting of the DL model, except for some grids near the boundaries, the density of the 11 903 models with different shapes was approximately 7000–8000 times per grid on average (see Fig. 2).

B. Structure of ResUnet Network

We use a CNN with an end-to-end learning network structure, where the 2-D observed anomalous gravity and GG data are considered inputs, and the 3-D anomalous density models are treated as training labels. The loss function is crucial in obtaining the perturbation of the weights and thresholds within the network. The loss function of the ψth training set is defined as $\boldsymbol{E}(\psi)$, using the root mean square error as

$$\boldsymbol{E}(\psi) = \sqrt{\frac{1}{n}\sum\nolimits_{i=1}^{n}(\rho_i - \bar{\rho}_i)^2} \tag{1}$$

where ρ_i and $\bar{\rho}_i$ represent the true and predicted values of the unit density of the anomalies, respectively.

In this article, we choose the ResUnet architecture for training the networks, whose structure is shown in Fig. 3(a). Different input features are incorporated in the network structure throughout encoding (left) and decoding (right) to improve the accuracy of prediction.

In the encoding part, a convolution residual block (Conv block) and an identity block are assembled within each step, where the output from the previous layer provides the feature extraction in the two-way forms [see Fig. 3(b)]. One is termed a direct connection, where the Conv block offers the function extracting the local features of the input throughout three convolution layers by implementing the Hadamard product of the gravity feature matrixes with the convolutional kernel (3×3) shown in Fig. 3(b). We chose the stride length as 1 to enhance the utilization efficiency of gravity and GG field anomaly. The identity block is responsible for taking out some portion of complexity input before the convolution through a shortcut marked as a blue arc shown in Fig. 3 and summing these with the features extracted by the subsequent Conv block before trigging rectified linear unit (ReLu) active function [50]. Unlike the Conv block, there is no convolution layer in the shortcut path shown in Fig. 3(b). The identity block is only available if the output and input share the same shape; alternatively, linear projection is applied. Furthermore, to suppress redundant information from the extracted feature maps and compress the dimension of the features, we use a $2 \times 2 \times 2$ maximum pooling block [51] to keep translation and stretching invariances for passing effective outputs further down.

In the decoding path, each step comprises a $2 \times 2 \times 2$ up-sampling block, a Conv block, and an identity block, which function to convert the extracted features back to the physical property value of the residual density model. The pooling operations during the encoding stage gradually lose the gravity image details. Therefore, the high-order gravity feature maps extracted during the encoding stage are integrated with the low-order feature map enlarged by the up-sampled response by concatenating, synthesizing composite features containing the spatial information and passing them down to the next layer [see Fig. 3(c)]. The concatenation, similar to the shortcut, allows for stacking deeper networks while avoiding degradation issues, ensuring network efficiency, and enhancing network performance. Compared to the encoding part, the decoding layer compensates for detailed information and can better retain the original features while achieving a good denoising effect.

III. Synthetic Model Studies

A. Model 1

This study employed a synthetic modeling scenario (Fig. 4) to serve as a reference and illustrate the challenges that may

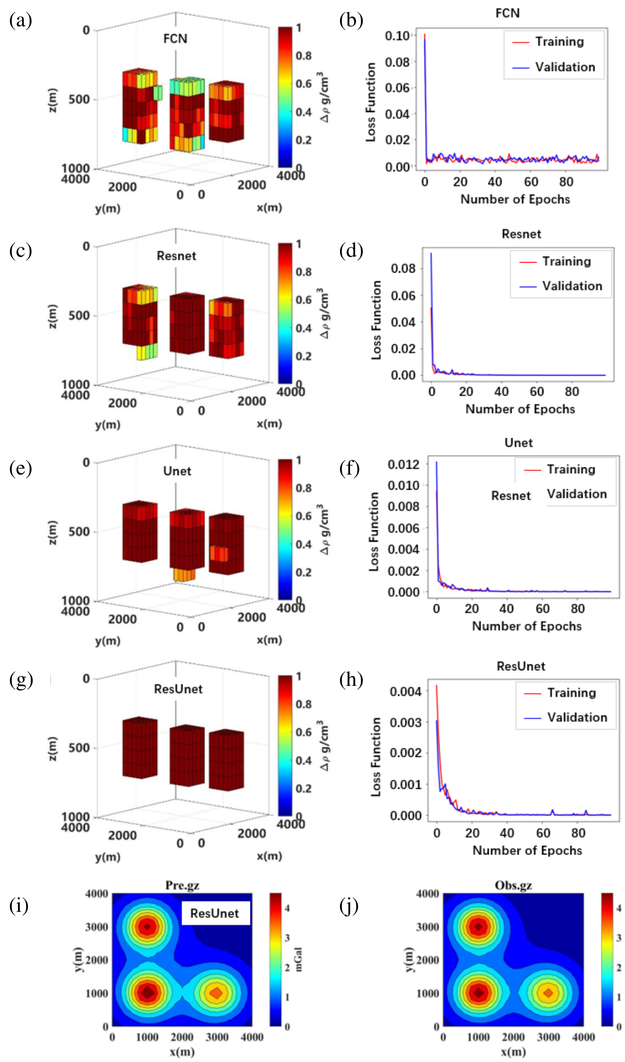

Fig. 5. (a) 3-D view model recovered by FCN network. (b) Learning history of FCN network. (c) 3-D view model recovered by ResNet network. (d) Learning history of ResNet network. (e) 3-D view model recovered by U-net network. (f) Learning history of U-net network. (g) 3-D view model recovered by ResUnet network. (h) Learning history of ResUnet network. (i) Predicted response by ResUnet network. (j) Observed response by ResUnet network.

TABLE I
LIST OF FITTING BEHAVIORS AND ERRORS ANALYSIS

	Param No.	Normalize Misfit	Max. Den. Errors	Max. Related . Errors	Training/inversion time cost
FCN	369822	0.0541	0.67	0.1669	23/ 00:04.8
Resnet	235050	0.0365	0.46	0.0688	44/00:05.1
U-net	441402	0.0271	0.19	0.004	32/00:05.0
ResUnet	942906	0.0091	0.01	0.0016	47/00:04.8

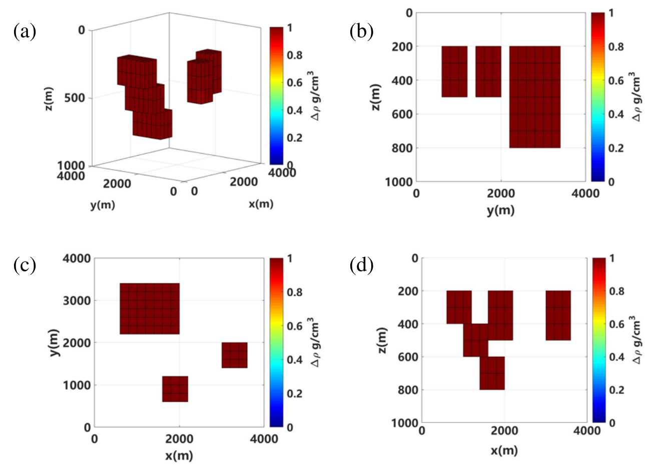

Fig. 6. (a) 3-D view of model 2. (b) Y–Z view of model. (c) X–Y view of the model. (d) X–Z view of the model.

arise when implementing conventional CNN architectures. The limitations identified in these conventional models motivated the assessment of the ResUnet architecture, which is presented in subsequent sections of this article.

Fig. 3 illustrates that the density anomalies predicted by the ResUnet network described in this study are consistent with the theoretical model, albeit with a certain density discrepancy, with an absolute density error range of 0.01–0.67 g/cm^3. Notably, the density model recovered by the ResUnet network [see Fig. 5(g)] is faithful to the synthetic model with a sharp boundary and accurately reflects the true density values (see Fig. 4), outperforming the results predicted by other networks [see Fig. 5(a), (c), and (e)]. The fitting between the predicted and observed data is demonstrated in Fig. 5(i) and (j), where the predicted gravity responses match well with the observed data. We should acknowledge that the ResUnet network constructed in this study has more hyperparameters than other networks, resulting in a prolonged training time. Nevertheless, after training, the network displays good robustness, requires less inversion time, and yields better results. A detailed summary of all cases in our synthetic study is presented in Table I, and the corresponding learning histories are shown in Fig. 5(c), (d), (f), and (h), respectively.

B. Model 2

Model 2 comprises a density dike and two cubic bodies with a top depth of 200 m, as illustrated in Fig. 6. To assess the stability of the trained ResUnet network when processing noisy data, we intentionally added independent Gaussian noise to each component of the gravity field with a mean of zero and standard deviation of 5%, 10%, and 15%. The gravity survey area ranges from 0 to 4000 m along the x- and y-axes. To reconstruct the density model, we implemented three strategies: 1) utilizing individual seven scalar components of the gravity and GG fields; 2) joining g_z, g_{xy}, g_{xz}, and g_{yz} components; and 3) integrating g_z, g_{zz}, g_{xx}, and g_{yy} components.

The reconstructed density models recovered from seven individual components (rows from top to bottom) contaminated by different noise levels (columns from left to right) are presented in Fig. 7. The trained ResUnet network is observed to capture the locations and shape of the density dike and the two cubic bodies accurately, avoiding smooth features and smeared-out boundaries that are typically produced by traditional smooth gravity inversion. The results indicate that the recovered density values of some inversion grids are randomly distributed based on some components, such as g_z, g_{xy}, and g_{yy}, with the increase of noise level contamination.

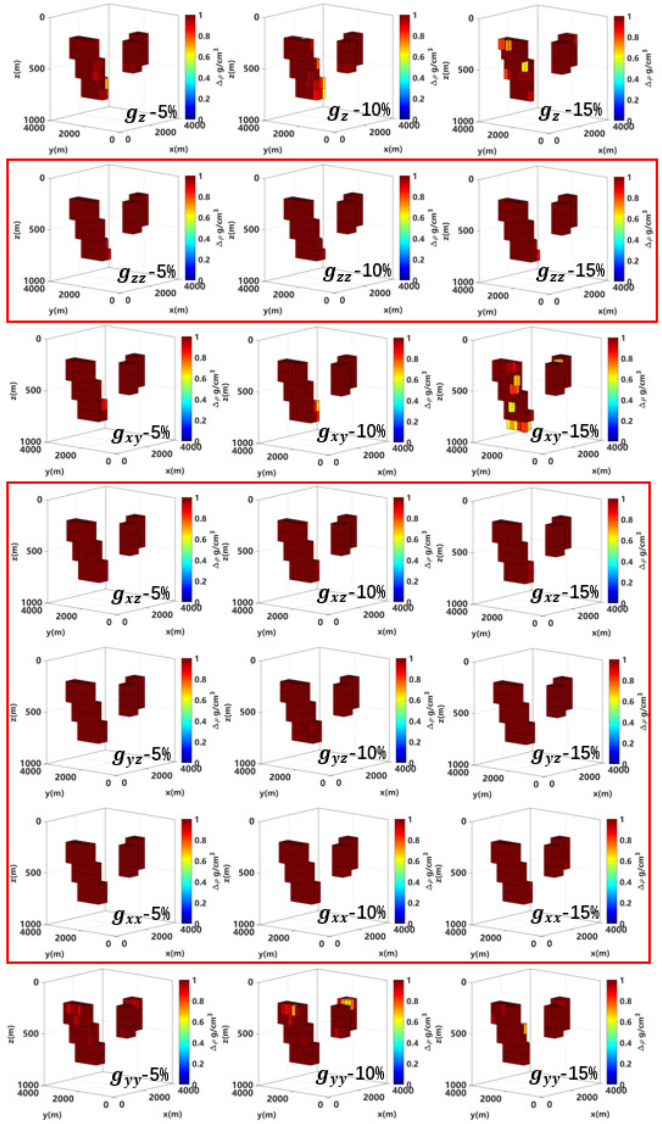

Fig. 7. (Top-down) present inverted models recovered from independent g_z, g_{zz}, g_{xy}, g_{xz}, g_{yz}, g_{xx}, and g_{yy}, respectively. (Left-right) depict the inverted models with 5%, 10%, and 15% random noise, respectively.

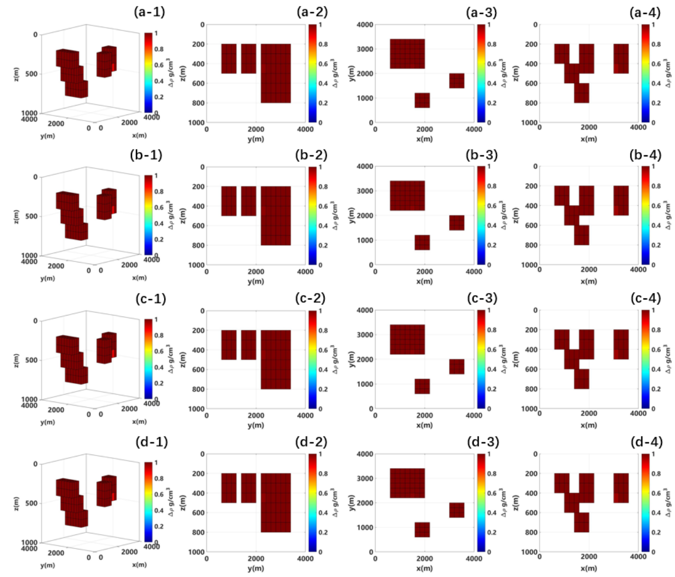

Fig. 8. Rows (top-down) present inverted models for joint components (g_z, g_{xy}, g_{xz}, and g_{yz}) without noise and with 5%, 10%, and 15% random noise, respectively. (a-1)–(d-1) depict 3D view, (a-2)–(d-2) Y–Z view, (a-3)–(d-3) X–Y view, and (a-4)–(d-4) X–Z view of the inverted model, respectively.

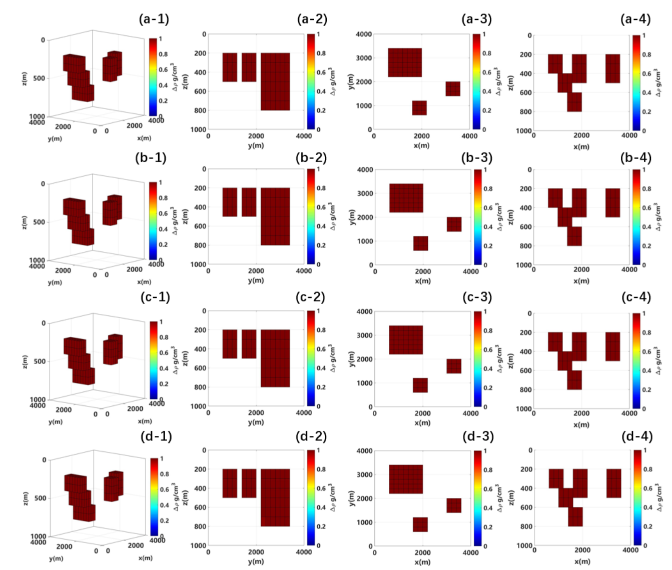

Fig. 9. Rows (top-down) present inverted models for joint components (g_z, g_{xx}, g_{yy}, and g_{zz}) without noise and with 5%, 10%, and 15% random noise, respectively. (a-1)–(d-1) depict 3D view, (a-2)–(d-2) Y–Z view, (a-3)–(d-3) X–Y view, and (a-4)–(d-4) X–Z view of the inverted model, respectively.

In contrast, the recovered density values derived from the remaining components (circled as a solid red rectangle) exhibit good stability and accuracy, being much closer to the true value.

Figs. 8 and 9 depict the recovered anomalous density models resulting from two distinct joint components (g_z–g_{xy}–g_{xz}–g_{yz} and g_z–g_{xx}–g_{yy}–g_{zz}) that were contaminated by varying levels of noise and processed by the trained ResUnet network. In comparison to the outcomes derived from individual components displayed in Fig. 7, the inverted models obtained from the joint components exhibit improved noise resistance and precision regarding both the spatial density distribution and the inverted density values.

Fig. 10 displays the rose diagrams for the normalized misfit obtained from the models recovered by individual components (see Fig. 7) and the two different joint components (see Figs. 8 and 9) against various levels of random noise, i.e., free-noise, 5%, 10%, and 15%. The results show that the increase in noise level decreases the closeness of fitting of g_z, g_{yy}, and, g_{xy}, leading to a relatively weaker model recovery ability in the validation stage, as observed in Fig. 8. Second, the fitting of the joint components (red and green) is better than that obtained by independent inversions (solid black line) for all noise scenarios, as seen in Fig. 10(b)–(d). Therefore, the model recovered from multicomponent data (see Figs. 8 and 9) is more consistent with the actual model than those obtained from individual components shown in Fig. 7. Moreover, the density models reconstructed by the two joint components are almost identical. These results suggest that the well-trained DL network model can automatically extract features from the data with noise, which has a negligible effect on the inversion results.

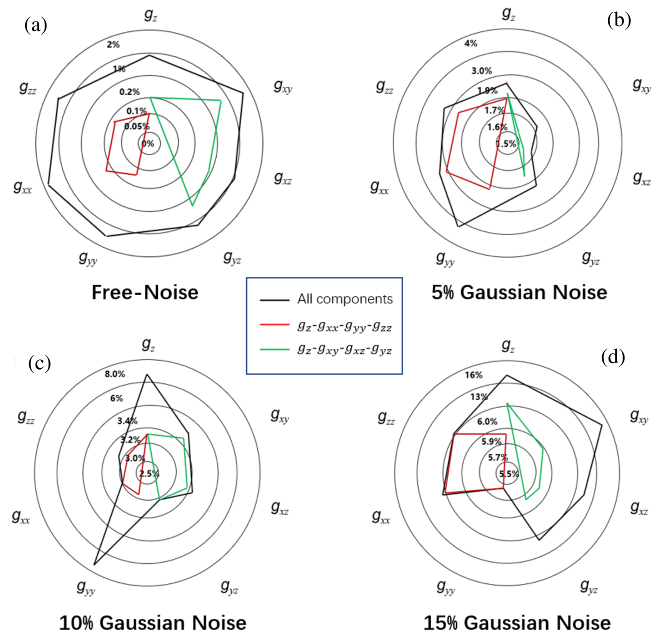

Fig. 10. Rose diagrams for the normalized misfit derived from the models recovered by the individual, and the two different joint components against (a) free-noise, (b) 5%, (c) 10%, and (d) 15%, respectively.

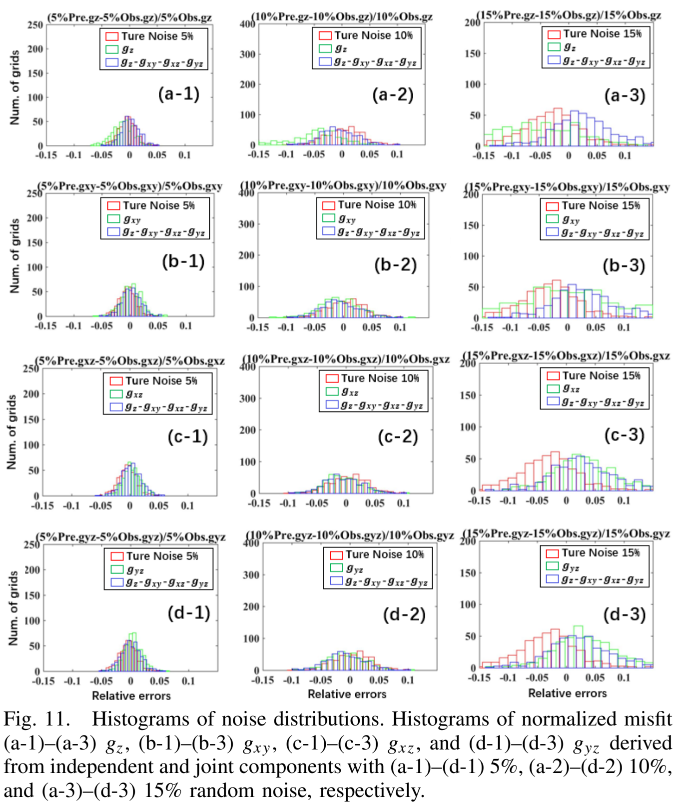

Fig. 11. Histograms of noise distributions. Histograms of normalized misfit (a-1)–(a-3) g_z, (b-1)–(b-3) g_{xy}, (c-1)–(c-3) g_{xz}, and (d-1)–(d-3) g_{yz} derived from independent and joint components with (a-1)–(d-1) 5%, (a-2)–(d-2) 10%, and (a-3)–(d-3) 15% random noise, respectively.

To evaluate the denoising capability of the trained ResUnet network, we conducted a separate analysis of the noise data by subtracting the predicted data based on different recovered models with varying random noise levels. The histograms of noise distributions are presented in Figs. 11 and 12, where the red color represents the true noise, the green color shows the individual components, and the blue color displays the two joint components as g_z–g_{xy}–g_{xz}–g_{yz} (see Fig. 11) and g_z–g_{xx}–g_{yy}–g_{zz} (see Fig. 12), respectively. The results show

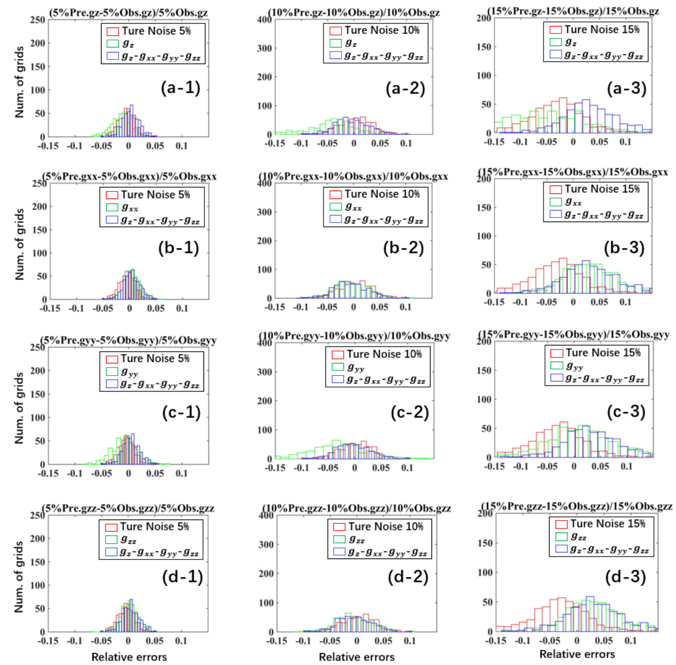

Fig. 12. Histograms of noise distributions. Histograms of normalized misfit (a-1)–(a-3) g_z, (b-1)–(b-3) g_{xx}, (c-1)–(c-3) g_{yy}, and (d-1)–(d-3) g_{zz} derived from independent and joint components with (a-1)–(d-1) 5%, (a-2)–(d-2) 10%, and (a-3)–(d-3) 15% random noise, respectively.

that for most gravity components with different noise levels, the distribution of intercepted noise data is approximately the same as the true distribution, with a mean of 0 and standard deviation of 5%, 10%, and 15%, respectively. This suggests that, compared to individual components, the trained ResUnet network demonstrates more stable anti-noise performance when carrying out the inversion of joint components. However, for the g_z, g_{xy}, and g_{yy} components, their noise distributions with a mean of around -0.05 exhibit certain discrepancies.

IV. Case Study

A. Geological Characteristic of the Area of a 3-D Marine FTG Survey

The full-tensor gradient (FTG) survey was conducted in the Nordkapp Basin located in the Barents Sea offshore Norway [see Fig. 11(a)]. The Nordkapp Basin can be further subdivided into two regions: the southwestern part (SWP) and the northeastern part (NEP). The SWP sub-basin (Obelix survey location) is a narrow, northeast-trending geological structure extending over a distance of 150 km and has a width of 25–50 km [52]. It encompasses more than 17 complex salt diapirs that represent the major geological structures in the area [see Fig. 13(b)]. On the other hand, the NEP sub-basin covers an area of 200 km in length and has a width of 50–70 km, and it includes over 16 salt structures. Hydrocarbon exploration in the Nordkapp basin commenced in the 1980s. Currently, three wells have been drilled on the flanks of the basin. Recent geological and geophysical explorations indicate that hydrocarbon reservoir discovery within the Nordkapp basin has the potential for success, with promising results outside the basin.

The main geological targets in the Nordkapp Basin in the Barents Sea are the salt diapirs G2 and F2. These targets

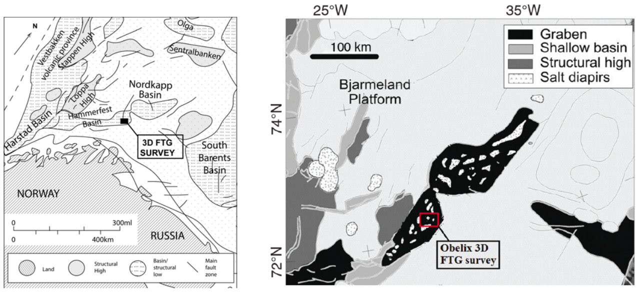

(a) (b)

Fig. 13. Geological maps in the Barents Sea area. (a) Main structural elements in the Barents Sea area, location of Nordkapp Basin and 3-D FTG survey. Modified from Johansen et al., 1993. (b) Simplified structural map of the Nordkapp basin showing salt diapirs and main fault zones. Black zones show subcrops of diapirs at or near the Pliocene-Pleistocene unconformity. Modified from Zhdanov and Lin [25].

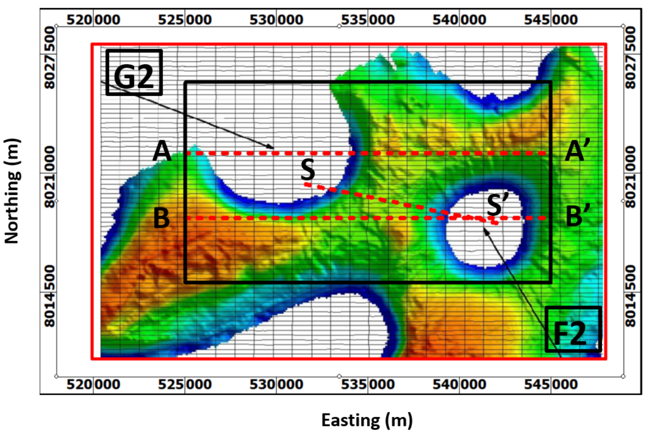

Fig. 14. Obelix 3-D FTG Survey Grid with Seismic Horizons. The main geological targets are the salt diapirs G2 and F2, which are manifested by the absence of well-resolved seismic horizons. The area remarked by solid red line is the original FTG survey grid. The subset marked by solid black line of the original FTG data focuses on the two salt diapir areas (G2 and F2). Two profiles A–A′, B–B′, and one seismic line is represented S-S′ by the red dashed line.

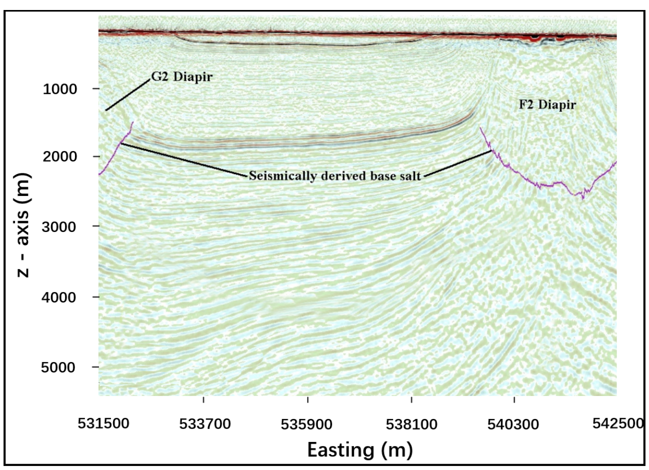

Fig. 15. Seismic Trace (S–S′) depth migrated profile from 3-D survey showing salt feature G2 and F2 and typical imaging ambiguity of high resolution seismic. The solid purple line represents interpreted salt edge derived from seismic. The interpreted edges were provided by Statoil without any detailed information.

are difficult to image with seismic horizons due to their complex geometries (see Fig. 14). Although seismic tools have advanced, the interpretation of salt structure remains challenging due to the underdetermined inversion models of the salt isopach (see Fig. 15). To address this, the FTG

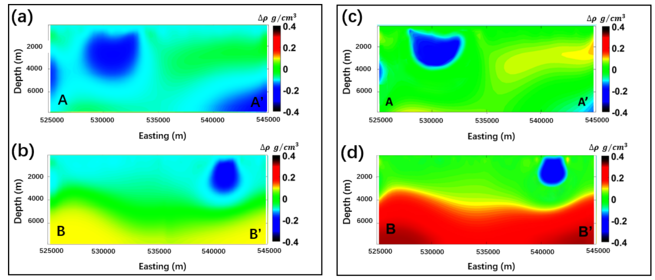

Fig. 16. Vertical slices of the inversion results along the profiles A–A′ and B–B′, respectively. (a–b) using the traditional smooth inversion and (c–d) using the ResUnet network.

survey was conducted to provide additional information on the complex salt overhang structures. FTG is a suitable solution for such problems since it is highly sensitive to geological anomalies with significant density contrasts. Statoil offers two types of salt base interpretation, one derived from seismic data marked by a solid purple line, and the other from FTG data marked by the red dashed line, which will be used to recognize and validate the inversion results.

To overcome these challenges, a rigorous 3-D inversion of the FTG data must be implemented. Previous publications have used focusing regularization for sharp boundary inversion of the FTG data in the Nordkapp Basin [11], [18], [53]. In this article, we present preliminary results of inversion using ResUnet, which is capable of establishing the relationship between labels, geological models, trained data, and predicted data to resolve sharp density contrasts between salt structures and the surrounding host rock.

B. Results

In Fig. 14, the FTG survey area is delineated by the solid red line. As the primary geological targets are the salt diapirs G2 and F2, we have chosen a subset of the FTG data from the original data set to concentrate on these two salt diapir regions marked by the solid black lines. The receivers were positioned at 300 m intervals along survey lines laid out along the Eastern region, with a separation of 300 m. We present the inversion outcomes as vertical sections along profiles A–A′, B–B′, and seismic profile S–S′.

Referring to the noise distribution analysis of the synthetic study, we have applied the well-trained ResUnet network by feeding the four components of FTG data: g_{xx}, g_{xz}, g_{yz}, and g_{zz}, neglecting g_z, g_{xy}, and g_{yy}. We have selected a modeling domain of 20 km (east-west, x-axis) $\times$ 11 km (north-south, y-axis) and continued until at a depth of 8 km (z-axis). The vertical discretization increases logarithmically from 100 m near the surface to 500 m at the bottom. This volume of inversion was discretized in $55 \times 32 \times 32 = 56\,320$ cells, and the selected modeling domain may represent a salt base or a deeper source down to approximately 8 km for salt structures F1 and G2. The total training time is approximately 55 min and the prediction time is around 7 s. For comparison, we implemented traditional smooth inversion to compare with the DL algorithm.

Fig. 16 shows the two inversion results using the four components in the form of vertical sections along the profiles A–A′ and B–B′, respectively. Fig. 16(c) and (d), show the

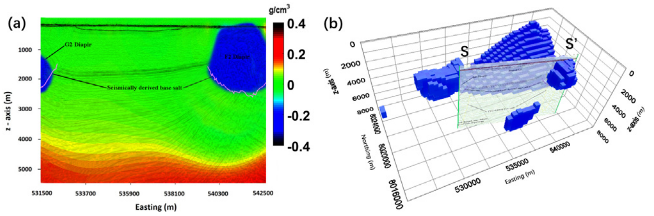

Fig. 17. Vertical slices of the inversion results along the profiles S–S′ and 3-D view, respectively. (a) Seismic profile S–S′ overlaps with a cross section of the inversion result using the ResUnet network and (b) 3-D view of the reconstructed density model.

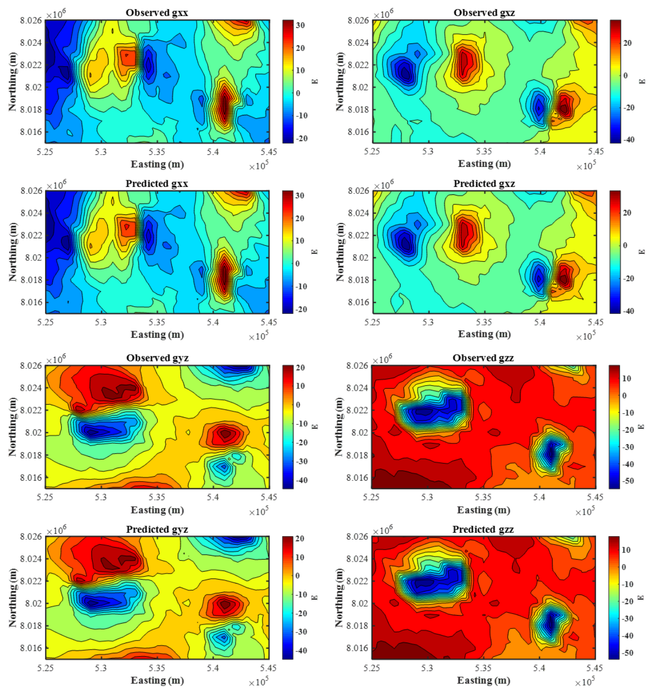

Fig. 18. Map of the observed and predicted data for the six components of FTG data: g_{xx}, g_{xz}, g_{yz}, and g_{zz}.

clear salt diapirs G2 and F2 geometry with a sharp boundary between salt diapirs and host rock, the model reconstructed by the ResUnet network. In contrast, the density model recovered by the typical smooth inversion in Fig. 14(a) and (b) is characterized by smooth features and smeared-out boundaries. Note that the focusing inversion results presented in [53] also show the sharp boundaries of the salt diapers.

To validate the accuracy of the results and make a comparison with inversion results produced by different methods, we project two 2-D vertical cross sections of inverted density contrasts along the corresponding seismic trace S–S′ profile in Fig. 17(a). The model reconstructed from the trained ResUnet network shows that the bottom edge of the salt diapir (F2) with relatively sharp density contrast is close enough to the interpreted ambiguity salt edge (solid purple line) derived from seismic. The 3-D view of the reconstructed density model is shown in Fig. 15(b). One can see that the geometry of two salt diapirs F2 and G2 can be clearly identified using the trained ResUnet network.

A comparison between observed and predicted FTG data is shown in the Fig. 18. One can see that for the four FTG components, the agreement between the predicted and the observed data is still very good. An average misfit between the observed and predicted data is around 7.5% which was the same as used as termination criteria by Zhdanov and Lin [25]. It was reached in about 20 iterations.

Nevertheless, it is relevant to note that the exclusive dependence on density contrasts as the singular rock parameters for characterizing gravity gradiometric anomalies imposes certain constraints. Specifically, the densification of sediments with increasing depth produces a so-called "nil zone" [54], characterized by an absence of contrasts in which the densities of both salt and sedimentary rocks are similar [47], [55]. It should be noted that while our study is focused on density variations, with which gravity inversion relies on apparent density contrast to estimate the subsurface distribution of mass. Examining layer variations presents a promising direction for future research to address the issue of destructive interference generated by the presence of salt bodies above and below the nil zone, which may result in gravity anomalies of opposing directions.

V. Conclusion

The ResUnet Network has shown great potential for applications in geophysical data analysis, structural reconstruction, and inversion. It allows for establishing the relationship between models and observed data without revealing the underlying mathematical equations and physical laws. The ResUnet network presented in this article was able to quickly establish this relationship and improve the accuracy and speed of subsurface physical property imaging.

To validate the proposed ResUnet inversion network, we used two synthetic models with uniform density contrast. The trained ResUnet network effectively recovered the detailed structures of isolated density anomalies and honored the true density values of models. Additionally, the recovered models from multicomponent data showed more consistency with the actual model than those produced by single-component data, demonstrating the importance of multicomponent gravity measurements in practical applications.

In practical applications, the ResUnet effectively predicted the geometry and density of the salt diapirs in the Nordkapp basin. The model reconstructed from the trained ResUnet network shows that the boundaries of the salt diapir (F2) with relatively sharp density contrast are close enough to the interpreted salt boundaries from seismic interpretation. These results highlight the potential of the ResUnet network in accurately characterizing subsurface geological structures.

Acknowledgment

The authors would like to thank the Changchun University of Science and Technology and the Chengdu University of Technology. They also would like to acknowledge the Engineering Geology Brigade of Jiangxi Bureau of Geology and Jiangxi Institute of Shale Gas Investigation and Development Research for providing the gravity and related data. The FTG data were collected by BellGeospace and made available by Equinor (former Statoil).

REFERENCES

[1] D. L. Alumbaugh and G. A. Newman, "Image appraisal for 2-D and 3-D electromagnetic inversion," *Geophysics*, vol. 65, no. 5, pp. 1455–1467, Sep. 2000.

[2] M. S. Zhdanov, P. Ellis, and S. Mukherjee, "Three-dimensional regularized focusing inversion of gravity gradient tensor component data," *Geophysics*, vol. 69, no. 4, pp. 925–937, Jan. 2004.

[3] M. Čuma, G. A. Wilson, and M. S. Zhdanov, "Large-scale 3D inversion of potential field data," *Geophys. Prospecting*, vol. 60, no. 6, pp. 1186–1199, Nov. 2012.

[4] M. Čuma and M. S. Zhdanov, "Massively parallel regularized 3D inversion of potential fields on CPUs and GPUs," *Comput. Geosci.*, vol. 62, pp. 80–87, Jan. 2014.

[5] M. Cuma and M. S. Zhdanov, "Continental-scale joint inversion of Alaska and Yukon gravity and magnetic data," *First Break*, vol. 35, no. 9, Sep. 2017.

[6] M. S. Zhdanov, *Geophysical Inverse Theory and Regularization Problems*. Amsterdam, The Netherlands: Elsevier, 2002.

[7] M. S. Zhdanov, *Inverse Theory and Applications in Geophysics*. Amsterdam, The Netherlands: Elsevier, 2015, p. 799.

[8] M. H. Dransfield and T. Chen, "Heli-borne gravity gradiometry in rugged terrain," *Geophys. Prospecting*, vol. 67, no. 6, pp. 1626–1636, Jul. 2019.

[9] Z. Meng, F. Li, D. Zhang, X. Xu, and D. Huang, "Fast 3D inversion of airborne gravity-gradiometry data using Lanczos bidiagonalization method," *J. Appl. Geophys.*, vol. 132, pp. 211–228, Sep. 2016.

[10] C. A. Mendonça, "Inversion of gravity-field inclination to map the basement relief of sedimentary basins," *Geophysics*, vol. 69, no. 5, pp. 1240–1251, Sep. 2004.

[11] X. Tu and M. S. Zhdanov, "Joint focusing inversion of marine controlled-source electromagnetic and full tensor gravity gradiometry data," *Geophysics*, vol. 87, no. 5, pp. K35–K47, Sep. 2022.

[12] Z. Zhang and M. Brand, "Convergent block coordinate descent for training tikhonov regularized deep neural networks," in *Proc. Adv. Neural Inf. Process. Syst.*, vol. 30, 2017.

[13] A. N. Tikhonov and V. I. Arsenin, *Solutions of Ill-Posed Problems*. Washington, DC, USA: Winston, 1977.

[14] C. Zhao, P. Yu, and L. Zhang, "A new stabilizing functional to enhance the sharp boundary in potential field regularized inversion," *J. Appl. Geophys.*, vol. 135, pp. 356–366, Dec. 2016.

[15] O. Portniaguine and M. S. Zhdanov, "Focusing geophysical inversion images," *Geophysics*, vol. 64, no. 3, pp. 874–887, May 1999.

[16] M. Rezaie, "3D non-smooth inversion of gravity data by zero order minimum entropy stabilizing functional," *Phys. Earth Planet. Interiors*, vol. 294, Sep. 2019, Art. no. 106275.

[17] P. Qin, D. Huang, Y. Yuan, M. Geng, and J. Liu, "Integrated gravity and gravity gradient 3D inversion using the non-linear conjugate gradient," *J. Appl. Geophys.*, vol. 126, pp. 52–73, Mar. 2016.

[18] Z. Xu, L. Wan, and M. S. Zhdanov, "Focusing iterative migration of gravity gradiometry data acquired in the nordkapp basin, Barents Sea," *Geophys. Prospecting*, vol. 68, no. 7, pp. 2292–2306, Sep. 2020.

[19] G. Zhao et al., "Efficient 3-D large-scale forward modeling and inversion of gravitational fields in spherical coordinates with application to lunar mascons," *J. Geophys. Res., Solid Earth*, vol. 124, no. 4, pp. 4157–4173, Apr. 2019.

[20] D. Venkataramani, R. J. Musgrave, D. A. Boutelier, A. C. Hack, and W. J. Collins, "Revised potential field model of the Gilmore fault zone," *Explor. Geophys.*, vol. 49, no. 4, pp. 572–583, Aug. 2018.

[21] Y. Junyan, X. Zhou, S. Yi, and W. Sun, "Determining dislocation love numbers using GRACE satellite mission gravity data," *Geophys. J. Int.*, vol. 203, no. 1, pp. 257–269, Oct. 2015.

[22] S. Vatankhah, R. A. Renaut, and V. E. Ardestani, "Total variation regularization of the 3-D gravity inverse problem using a randomized generalized singular value decomposition," *Geophys. J. Int.*, vol. 213, no. 1, pp. 695–705, Apr. 2018.

[23] Z. Xu et al., "3-D hybrid imaging based on gravity migration and regularized focusing inversion to predict the Poyang basin interface," *Geophysics*, vol. 86, no. 4, pp. 1–46, 2021.

[24] J. Sun and Y. Li, "Multidomain petrophysically constrained inversion and geology differentiation using guided fuzzy *c*-means clustering," *Geophysics*, vol. 80, no. 4, pp. ID1–ID18, Jul. 2015.

[25] M. S. Zhdanov and W. Lin, "Adaptive multinary inversion of gravity and gravity gradiometry data," *Geophysics*, vol. 82, no. 6, pp. G101–G114, Nov. 2017.

[26] Z. Xu, G. Zou, Q. Wei, J. Tian, and H. Yuan, "Focusing joint inversion of gravity and magnetic data using a clustering stabilizer in a space of weighted parameters," *Geophys. J. Int.*, vol. 224, no. 2, pp. 1344–1359, Oct. 2020.

[27] Y. Li and J. Sun, "3D magnetization inversion using fuzzy c-means clustering with application to geology differentiation," *Geophysics*, vol. 81, no. 5, pp. J61–J78, Sep. 2016.

[28] E. Amirian, J. Y. Leung, S. Zanon, and P. Dzurman, "Integrated cluster analysis and artificial neural network modeling for steam-assisted gravity drainage performance prediction in heterogeneous reservoirs," *Exp. Syst. Appl.*, vol. 42, no. 2, pp. 723–740, Feb. 2015.

[29] S. M. Iveson, M. Mason, and K. P. Galvin, "Gravity separation and desliming of fine coal: Pilot-plant study using reflux classifiers in series," *Int. J. Coal Preparation Utilization*, vol. 34, no. 5, pp. 239–259, Sep. 2014.

[30] S. Chander and D. Ganguly, "Development of water level estimation algorithms using SARAL/Altika dataset and validation over the Ukai reservoir, India," *Proc. SPIE*, vol. 11, no. 1, Jan. 2017, Art. no. 016012.

[31] A. S. Harvey and G. Fotopoulos, "Geological mapping using machine learning algorithms," in *Proc. 33rd ISPRS Congr., Commission*, vol. 41, no. B8, 2016, pp. 423–430.

[32] S. Zhu, B. Hrnjica, J. Dai, and B. Sivakumar, "RETRACTED: Machine learning approaches for estimation of sediment settling velocity," *J. Hydrol.*, vol. 586, Jul. 2020, Art. no. 124911.

[33] G. Hu et al., "Mathematical vector framework for gravity-specific land surface curvatures calculation from triangulated irregular networks," *GIScience Remote Sens.*, vol. 59, no. 1, pp. 590–608, Dec. 2022.

[34] Y. Yao et al., "Mapping fine-scale population distributions at the building level by integrating multisource geospatial big data," *Int. J. Geograph. Inf. Sci.*, vol. 31, pp. 1220–1244, Jun. 2017.

[35] T. Pivetta and C. Braitenberg, "Sensitivity of gravity and topography regressions to earth and planetary structures," *Tectonophysics*, vol. 774, Jan. 2020, Art. no. 228299.

[36] X. Li et al., "Three-dimensional mineral prospectivity modeling for targeting of concealed mineralization within the Zhonggu iron orefield, Ningwu basin, China," *Ore Geol. Rev.*, vol. 71, pp. 633–654, Dec. 2015.

[37] M. H. Bencharef, A. M. Eldosouky, S. Zamzam, and D. Boubaya, "Polymetallic mineralization prospectivity modelling using multi-geospatial data in logistic regression: The diapiric zone, northeastern Algeria," *Geocarto Int.*, vol. 37, no. 27, pp. 15392–15427, Dec. 2022.

[38] G. Florio, "Mapping the depth to basement by iterative rescaling of gravity or magnetic data," *J. Geophys. Res., Solid Earth*, vol. 123, no. 10, pp. 9101–9120, Oct. 2018.

[39] Z. H. Zhang et al., "Deep learning for potential field edge detection," *Chin. J. Geophys.-Chin. Ed.*, vol. 65, no. 5, pp. 1785–1801, May 2022.

[40] A. M. Albora, A. Bal, and O. N. Ucan, "A new approach for border detection of the Dumluca (Turkey) iron ore area: Wavelet cellular neural networks," *Pure Appl. Geophys.*, vol. 164, no. 1, pp. 199–215, Jan. 2007.

[41] R. F. Annan and X. Wan, "Recovering bathymetry of the Gulf of Guinea using altimetry-derived gravity field products combined via convolutional neural network," *Surveys Geophys.*, vol. 43, no. 5, pp. 1541–1561, Oct. 2022.

[42] S. Zhao, D. Liu, Q. Yuan, and J. Li, "A global gravity reconstruction method for mercury employing deep convolutional neural network," *Remote Sens.*, vol. 12, no. 14, p. 2293, Jul. 2020.

[43] S. He, H. Cai, S. Liu, J. Xie, and X. Hu, "Recovering 3D basement relief using gravity data through convolutional neural networks," *J. Geophys. Res., Solid Earth*, vol. 126, no. 10, Oct. 2021.

[44] W. K. Hastings, "Monte Carlo sampling methods using Markov chains and their applications," *Biometrika*, vol. 57, no. 1, pp. 97–109, Apr. 1970.

[45] D. Blatter, K. Key, A. Ray, N. Foley, S. Tulaczyk, and E. Auken, "Trans-dimensional Bayesian inversion of airborne transient EM data from Taylor glacier, Antarctica," *Geophys. J. Int.*, vol. 214, no. 3, pp. 1919–1936, Jul. 2018.

[46] N. P. Agostinetti and A. Malinverno, "Receiver function inversion by trans-dimensional Monte Carlo sampling," *Geophys. J. Int.*, vol. 181, no. 2, pp. 858–872, 2010.

[47] X. Wei, J. Sun, and M. K. Sen, "Quantifying uncertainty of salt body shapes recovered from gravity data using trans-dimensional Markov chain Monte Carlo sampling," *Geophys. J. Int.*, vol. 232, no. 3, pp. 1957–1978, Nov. 2022.

[48] A. Kelbert, G. D. Egbert, and C. deGroot-Hedlin, "Crust and upper mantle electrical conductivity beneath the Yellowstone hotspot track," *Geology*, vol. 40, no. 5, pp. 447–450, May 2012.

[49] S. Maiti and R. K. Tiwari, "Neural network modeling and an uncertainty analysis in Bayesian framework: A case study from the KTB borehole site," *J. Geophys. Res.*, vol. 115, no. B10, 2010.

[50] B. Xu, N. Wang, T. Chen, and M. Li, "Empirical evaluation of rectified activations in convolutional network," 2015, *arXiv:1505.00853*.

[51] Y.-L. Boureau et al., "Learning mid-level features for recognition," in *Proc. IEEE Comput. Soc. Conf. Comput. Vis. Pattern Recognit.*, Jun. 2010, pp. 2559–2566.

[52] K. T. Nilsen, B. C. Vendeville, and J. T. Johansen, "Influence of regional tectonics on halokinesis in the Nordkapp Basin, Barents Sea," *Salt Tectonics, A Global Perspective*, vol. 65, pp. 413–436, 1995.

[53] L. Wan and M. S. Zhdanov, "Focusing inversion of marine full-tensor gradiometry data in offshore geophysical exploration," in *Proc. SEG Tech. Program Expanded Abstr.*, 2008, pp. 751–755.

[54] P. A. Allen and J. R. Allen, *Basin Analysis: Principles and Application To Petroleum Play Assessment*. Hoboken, NJ, USA: Wiley, 2013.

[55] E. Ghalenoei, J. Dettmer, M. Y. Ali, and J. W. Kim, "Gravity and magnetic joint inversion for basement and salt structures with the reversible-jump algorithm," *Geophys. J. Int.*, vol. 227, no. 2, pp. 746–758, Jul. 2021.

Zhengwei Xu received the M.Sc. degree in geo-exploration science and information technology from Jilin University, Changchun, China, in 2008, and the Ph.D. degree in geophysics from the University of Utah, Salt Lake City, UT, USA, in 2013.

He is currently a Researcher with the College of Geophysics, Chengdu University of Technology, Chengdu, China. His research interests include gravity, magnetic, and electromagnetic forward modeling and inversion theory, as well as incorporation and joint inversion of multigeophysical data using artificial intelligence.

Rui Wang received the Ph.D. degree in traffic and transportation engineering from Jilin University, Changchun, China, in 2014.

He is currently an Associate Professor and Head of the Software Engineering Department, School of Computer Science and Technology, Changchun University of Science and Technology, Changchun. His main research interests include machine learning, computer vision, geophysics, and deep learning interpretation of continental dynamics.

Michael S. Zhdanov (Member, IEEE) received the M.Sc. degree in geophysics from the Moscow Gubkin State University of Oil and Gas, Moscow, Russia, in 1970, and the Ph.D. degree in physics and mathematics from Moscow State University, Moscow, in 1978.

He is currently a Distinguished Professor with the Department of Geology and Geophysics, The University of Utah, Salt Lake City, UT, USA, the Director of the Consortium for Electromagnetic Modeling and Inversion (CEMI), and the CEO and Chairman of TechnoImaging, Salt Lake City. He is also an Honorary Gauss Professor of the Göttingen Academy of Sciences, Göttingen, Germany, an Honorary Professor of the China National Centre for Geological Exploration Technology, Beijing, China. His research interests include fundamental and applied geophysics, inversion theory, electromagnetic theory, methods, and integration and joint inversion of multiphysics data.

Dr. Zhdanov is a fellow of the Russian Academy of Natural Sciences and Electromagnetics Academy USA, and an Honorary Member of the Society of Exploration Geophysicists.

Xuben Wang received the Ph.D. degree in geophysics from the College of Geophysics, Chengdu University of Technology, Chengdu, China, in 2002.

He is currently a Senior Professor with the College of Geophysics and also the Director of the Key Laboratory of Earth Exploration and Information Technology of the Ministry of Education, Chengdu University of Technology, the Executive Director of the Chinese Geophysical Society. He is also the Director of the Innovation Consortium for Geophysics and Continental Dynamics and the Senior Visiting Scholars of the Commonwealth Scientific and Industrial Research Organisation (CSIRO), Black Mountain, ACT, Australia. His main research interests include magnetotellurics and airborne electromagnetic forward and inversion theory as well as the multiphysics interpretation of continental dynamics.

Jun Li received the B.S., M.Sc., and Ph.D. degrees in geophysics from the Chengdu University of Technology, Chengdu, China, in 2001, 2005, and 2010, respectively.

His research interests include fundamental and applied geophysics, inversion theory, gravity, magnetic theory, and methods.

Bing Zhang received the B.S., and M.Sc., degrees from Yangtze University, Jingzhou, China, in 2004 and 2007, respectively, and the Ph.D. degree in geophysical prospecting and information technology from the Chengdu University of Technology, Chengdu, China, in 2010.

He is currently an Associate Researcher with the College of Geophysics, Chengdu University of Technology. His research interests in reservoir geology and petrophysics.

Shengxian Liang received the B.S. degree in geophysics from the China University of Geosciences, Wuhan, China. He is currently pursuing the Ph.D. degree with the Chengdu University of Technology, Chengdu, China.

His research interests include gravity and magnetic inversion imaging, geophysical exploration of solid minerals and oil and gas, and geodynamics.

Yang Wang received the B.S. and M.S. degrees from the Department of Geosciences, China University of Petroleum (East China), Qingdao, China, in 2010 and 2012, respectively, and the Ph.D. degree from the Department of Geophysics, University of Houston, Houston, TX, USA, in 2020.

He is currently an Associate Research Fellow with the Key Laboratory of Geophysics, SINOPEC Geophysical Research Institute, Nanjing, China. His research interests include rock physics and rock mechanics in porous media, geomechanics in unconventional reservoirs, well logging, and seismic interpretation.